JOURNAL OF MATERIALS SCIENCE 27 (1992) 399–407

TEM study of microstructure development during low-cycle fatigue of an overaged Al–Mg–Si alloy

M. JAIN*
Department of Mechanical Engineering, University of Manitoba, Winnipeg, Manitoba, Canada R3T 2N2

The evolution of dislocation structure during room-temperature, uniaxial, low-cycle fatigue of an overaged Al–Mg–Si alloy is studied. Ageing at 450 °C produces a fine dispersion of Mg_2Si precipitate particles. During fully reversed strain-controlled cyclic tests, these fine particles restrict deformation to local regions and a stable dislocation substructure is developed early in fatigue life. Substructural observations of hardening and saturation by transmission electron microscopy reveal extensive dislocation band formation on Mg_2Si precipitate rods. Various microstructural features such as configuration of tangled dislocations, dislocation cells, precipitate morphologies, sizes, precipitate-free zones, etc., have been examined during cyclic hardening and saturation. The results have been analysed in terms of kinematic and isotropic-type microstructural mechanisms.

1. Introduction

Evolution of dislocation substructure and dislocation–precipitate interactions during uniaxial low-cycle fatigue (ULCF) of aged high-strength aluminium alloys have been the subject of many recent studies [1–9]. In these studies, the formation of dislocation loops [9], slip bands [1, 4–6, 8], dislocation cells [3, 7], and the evolution of dislocation structure after ULCF have been observed by transmission electron microscopy (TEM). Two types of precipitate, depending upon the ageing characteristics of the alloys, are generally identified; shearable and non-shearable. The shearable precipitates in underaged to peak-aged condition, show cyclic hardening to a peak stress followed by cyclic softening [1], whereas the non-shearable precipitates result in cyclic hardening leading to saturation [10, 11]. The microstructural features have been related to the shape of the hysteresis loops [2, 4, 12], the stacking fault energy (SFE) [3], the strain amplitude [1, 2, 5, 6], and the cumulative strain (or number of cycles) [1, 2, 5, 8, 9].

There have been several investigations of precipitation and ageing characteristics of Al–Mg–Si alloys. These alloys in the solution-treated and underaged state contain a fine dispersion of β″ needle-like zones, which are coherent and lie along ⟨1 0 0⟩. A precipitate free zone (PFZ) is usually observed along the grain boundaries. The PFZs form due to the absence of a critical vacancy concentration for precipitate nucleation at the grain boundaries [13]. There are other dispersoids present and are linked to iron impurity and excess silicon. The peakaged and overaged alloys contain partially coherent rods of β′-Mg_2Si lying along ⟨1 0 0⟩, about 0.2 μm long and 0.01 μm wide. The rods are an intermediate phase and have a structure of highly ordered unit cell of Mg_2Si. The orientation relationship between the matrix aluminium and β′-Mg_2Si rods has been reported to be ⟨1 0 0⟩Al||⟨1 1 0⟩ β′-Mg_2Si [14, 15]. The growth of the needle-shaped zones into β′-Mg_2Si precipitate rods takes place by the diffusion of solute atom/vacancy groups into the compressive regions of the zones, i.e. along the matrix ⟨1 0 0⟩ directions [14–16]. The degree of ageing of the solution-treated alloy determines the size and the strength of the β′ rods and the width of the PFZs. The width of the PFZs and the size of the dispersoids are significantly larger than the underaged alloys. On further ageing, β′-Mg_2Si precipitate rods transform to β-Mg_2Si plates. High-cycle fatigue studies on Al–Mg–Si in various solution-treated and aged conditions have also been conducted to study the effect of thermomechanical treatment (TMT), microstructural characteristics, residual stresses on fatigue life. The results are analysed in terms of the effect of various shearable and non-shearable precipitates on slip localization, crack initiation, and propagation characteristics [17–20]. No studies have been made in the past with respect to the processes of interaction between dislocations and precipitates resulting from ULCF of overaged precipitates. This is important because extensive dislocation movement and interaction with non-deformable overaged Mg_2Si precipitates is expected to influence the development of microstructure and internal stresses in these alloys.

In the present work, an investigation of dislocation

Present address: Alcan International Limited, Kingston R and D Centre, Box 8400, Kingston, Ontario, Canada K7L 5L9.

0022–2461/92 $03.00 + .12

substructure evolution and dislocation–precipitate interaction is conducted in overaged Al–Mg–Si alloy specimens subjected to low-cycle fatigue. The qualitative microstructural observations are discussed and analysed in terms of established kinematic and isotropic microstructural mechanisms operative in different regions of the microstructure.

2. Experimental procedure

2.1. Material and heat treatment

Commercial Al–Mg–Si (6061 Al) bar was received in the form of a 12.7 mm diameter circular bar having a nominal composition of 0.94% Mg, 0.67% Si, 0.52% Fe, 0.27% Cu, and 0.31% Cr as alloying elements. The as-received microstructure of Al–Mg–Si alloy consisted of a uniform equiaxed grain size. The grain size determined by a linear intercept method was 70 μm. The material was solution treated at 530 °C, water quenched, and aged at 160 °C for 18 h, followed by air cooling. The resulting microstructure consisted predominantly of a fine dispersion of Mg_2Si zones. The specimens were further aged at 450 °C for 1 h to develop a coarse distribution of β′-Mg_2Si precipitate rods.

2.2. Fatigue testing

The specimens were subjected, in laboratory air, to strain-controlled uniaxial cyclic loading in a microprocessor-based, closed-loop, servo-controlled, electrohydraulic test machine of 89 kN capacity. The tests were conducted at a strain amplitude and strain rate of 0.005 and $1 \times 10^{-2}\,s^{-1}$, respectively, up to various numbers of cycles in the cyclic hardening and saturation region. The details of computer-controlled fatigue testing and measurement of internal stress variables and test results are being published separately [21].

2.3. Transmission electron microscopy

Specimens for TEM were obtained by spark cutting 3 mm diameter discs from sections of the gauge length perpendicular to the specimen axis. Slices about 1 mm thick were cut by a diamond saw and ground to about 0.25 mm thickness. Thin foils were made by electropolishing in a nitric acid–methanol mixture at −35 °C by double-jet technique using a Tenupol polisher operating at 20 V. The foils from undeformed and deformed specimens were examined in a Jeol 2000 FX electron microscope at 200 kV. Bright-field dislocation contrast was enhanced by tilting to various two-beam diffracting conditions. The precipitate size and morphologies were observed by tilting the foil away from the exact two beam case, thus minimizing the strain contrast. The approximate composition of various dispersoids was determined by energy dispersive X-ray analysis (EDXA) attached to TEM by obtaining a typical spectrum of the intensity (counts) as a function of energy.

3. Results

The solution treatment at 530 °C, water quenching, and ageing at room temperature for 18 h showed a large number of quenched-in dislocation loops (Fig. 1a). The microstructure after ageing at 160 °C for 18 h consisted of a fine dispersion of Mg_2Si zones in a matrix of aluminium (Fig. 1b).

The material was aged at 450 °C for 1 h to obtain bigger particles. The overaged microstructures consisted predominantly of elongated, ordered β′-Mg_2Si precipitate rods of width 0.02–0.05 μm and lengths up to 2 μm, as shown in Fig. 2a. The black spherical spots in Fig. 2a are the β′-Mg_2Si precipitate rods observed "end on" in the [0 0 1] direction. Occasionally a large precipitate plate oriented along the same direction as β′-Mg_2Si precipitate was observed (Fig. 2b). The

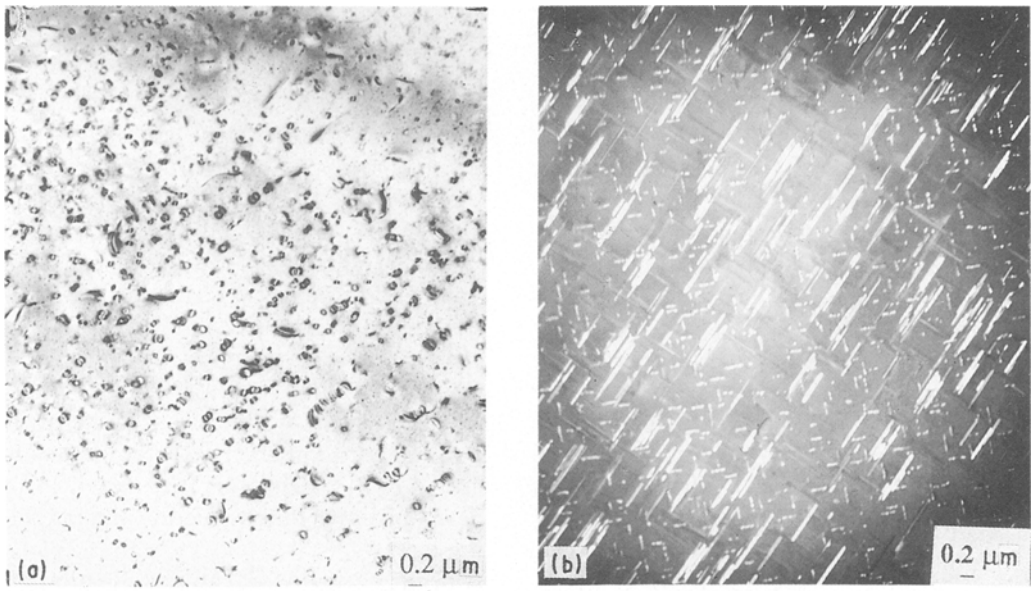

Figure 1 Transmission electron micrographs of the microstructures of solution-treated and aged specimens. (a) Solution treated at 530 °C, (b) solution treated as above and aged at 160 °C for 18 h.

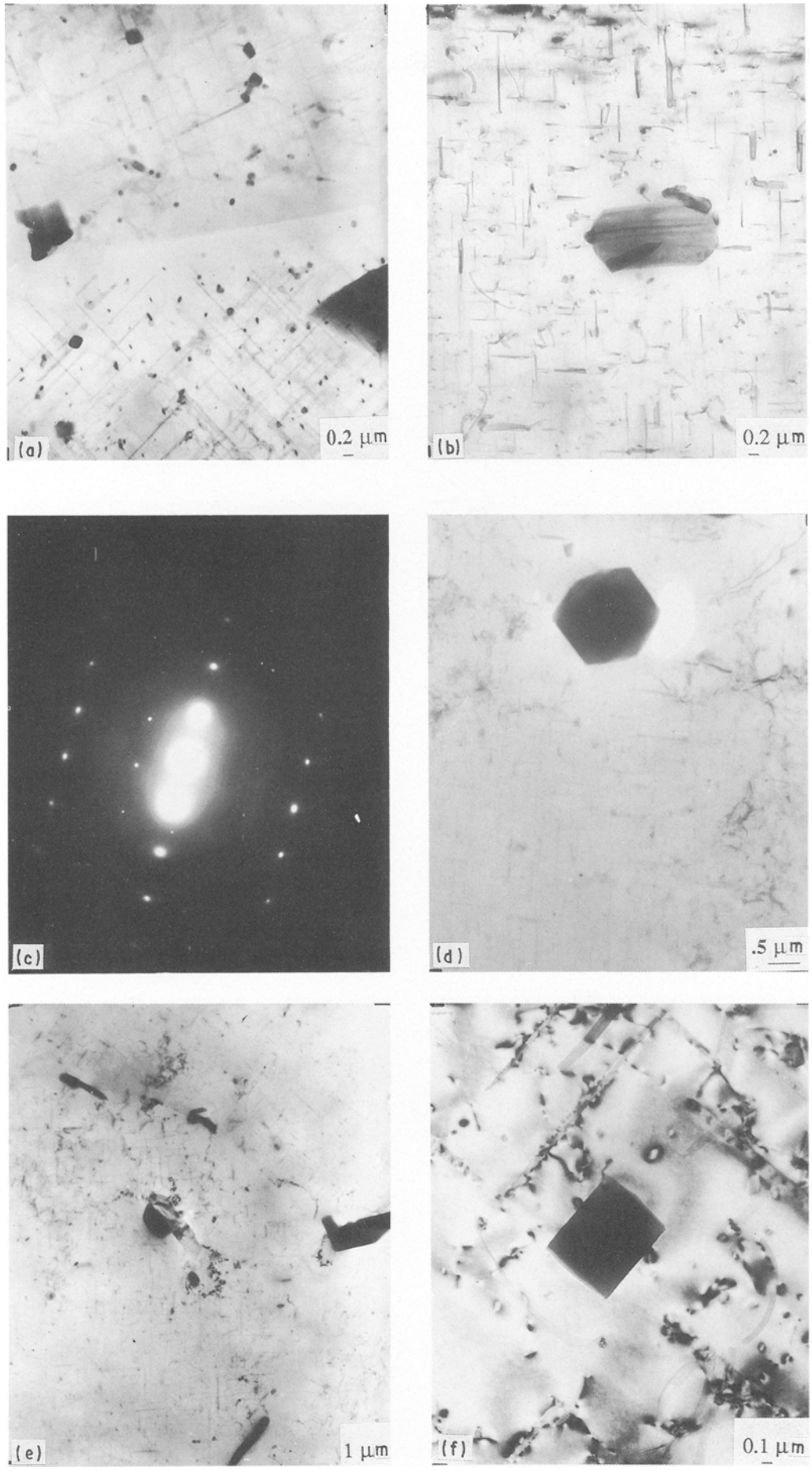

Figure 2 Transmission electron micrographs of a specimen in the overaged, undeformed, condition. (a) Cylindrical precipitate rods of β′-Mg_2Si in the matrix; (b) a large β-Mg_2Si precipitate plate; (c) diffraction pattern from a Mg_2Si precipitate rod; (d) a large polygonal precipitate particle in the grain interior; (e) irregular precipitates and PFZs along the grain boundaries; (f) dislocations at the Mg_2Si precipitates and a β precipitate plate.

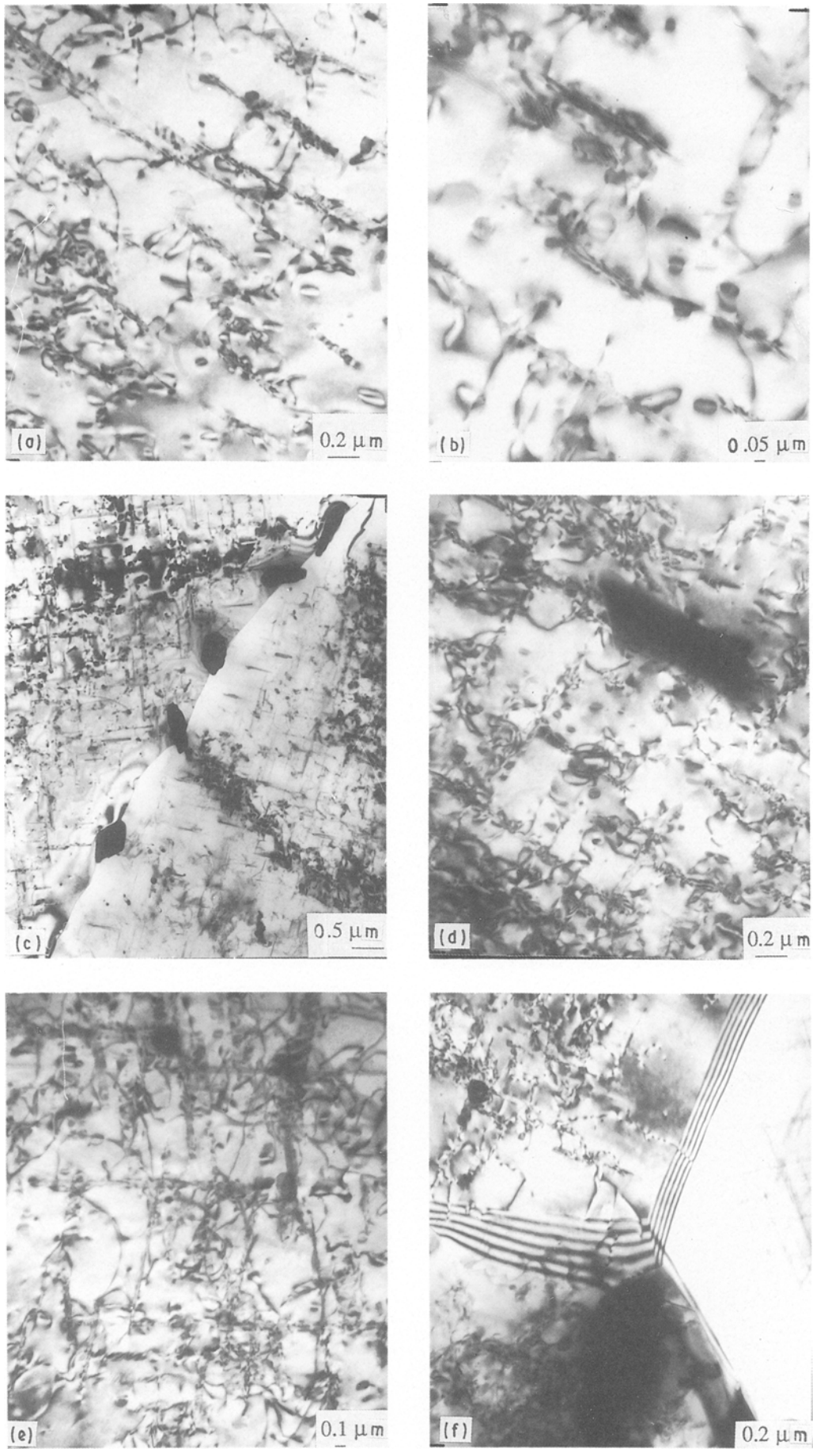

Figure 3 Transmission electron micrographs of cyclically deformed specimens in the cyclic hardening region at $\Delta\varepsilon/2 = 0.005$ and $\dot{\varepsilon} = 0.01\ s^{-1}$ after (a–c) two cycles, and (d–f) ten cycles.

dissolution of β′ rods in the areas surrounding the plate results in a precipitate-free region. The precipitate plates were identified by selected-area diffraction (SAD) and EDXA analysis in the TEM to be β-Mg_2Si. The diffraction pattern from the Mg_2Si precipitate plates indicated an f c c structure with a lattice parameter of 0.64 nm (Fig. 2c). Large precipitates of spherical, polygonal, cylindrical shapes were also observed in the grain interior (Fig. 2d and f). The sizes of the large precipitates varied considerably and were in the range 1–10 μm. A number of discretely distributed precipitates of arbitrary shapes and varying sizes were often encountered along the grain boundary as shown in Fig. 2e. The PFZs, 0.5–2.0 μm wide, were also observed along the grain boundaries and grain triple points as shown in Fig. 2a and e. In some cases, large particles also appeared to align themselves along certain crystallographic directions. The large precipitates were too thick to obtain a suitable diffraction pattern for analysis. The EDX analysis was therefore employed to identify the elements present in various precipitates. The analysis of large precipitates of polygonal geometry showed a distinct Si peak whereas the large spherical precipitates consisted of silicon, chromium, iron and aluminium. A small number of dislocations, nucleated during precipitation and ageing, were observed on the interface between the matrix and the β′ precipitate rods as well as other large precipitates (Fig. 2d and f). The small size of the β′ rods and the contrast associated with the large coherency strains present did not allow a close examination of the interaction between the dislocations and the β′ rods.

The microstructures after two cycles at a strain amplitude of 0.5% (strain rate $1 \times 10^{-2}\ s^{-1}$) during hardening show a build up of dislocation structure in the matrix (Fig. 3a and b). A large number of bowed dislocations with screw components are held up at β′ rods and other large precipitates (Fig. 3a). Dislocation multiplication results in increased dislocation activity in the channels between the β′ precipitates and a general tangling around β′ was observed. A significant number of dislocations in the form of dislocation loops and curved configurations lie between β′ precipitate rods which act as pinning points. Multiple jogs generate long dipoles which decompose into loops (Fig. 3b). The dislocation loops associated with the interfaces of the β′ rods are debris from a bypass process, i.e. they are Orowan loops. An array of precipitates along a pinned grain boundary and PFZ of varying width, as well as the dislocation structure in the interior of the grains, are shown in Fig. 3c. In general, the boundaries contained many particles but no boundary cavitation was observed. Fig. 3d–f show the bright-field transmission electron micrographs after 10 cycles. A perpendicular "grid-like" configuration of dislocations in the form of intersecting dislocation bands exists throughout the bulk of the grains except at the PFZs. As the β′ rods tend to homogenize effectively the deformation in the matrix phase, any cell structure formed is very poorly defined. In some cases, the dislocation band continued for long distances as a distinct feature of the microstructure but in others they were recognizable only because of a rather diffuse contrast. The dislocation arrangement is less dense and irregular in the PFZs. The dislocation bands coincide with the ordered arrangement of β′ precipitate rods (Fig. 3f).

Fig. 4 shows the microstructures after 30 cycles in the early stages of saturation. The matrix dislocations further fill the channels between the β′ rods and are stored at the precipitate–matrix interface (Fig. 4a). The cell-like dislocation structure is developed in the PFZs as shown by grain A in Fig. 4b. The dislocation structure in the PFZ of the grain B below is not visible due to the misorientation between the bulk of the grain and the PFZ but one can observe the ordered arrangement of precipitates below the PFZ boundary. In the interior of the grains, the dislocation bands are well established although many bowed out dislocations exist in the inter-band region (Fig. 4c). The arrangement of boundary fringes around pinned grain boundary AB suggests that the boundary appears more likely to be wrapped around the particle (P) than pass through it (also Fig. 3c). Because the orientation of the intersecting perpendicular dislocation bands was the same as the β′ precipitate rods, the slip bands had a different orientation from grain to grain. The gradient of dislocation density is sharply defined between dislocation band and inter-band region. The dislocation–precipitate networks terminate at PFZ boundaries (Fig. 4c and e). The dislocation structure in the vicinity of a β′ plate is marked by a more cellular dislocation configuration due to the absence of precipitate rods (Fig. 4d). The dislocation structure of a region free of β′ precipitates but in the vicinity of large dispersoids is shown in Fig. 4f.

Fig. 5 shows transmission electron micrographs of a specimen after 511 cycles. A complete saturation in the flow stress was observed at this stage. The β′ rods are now fully covered by dislocations (Fig. 5a and b). The dislocation–precipitate bands are more intense with a dense network of dislocation debris between the bands. A large number of dense dislocation tangles were also observed in the vicinity of large (> 1 μm) precipitates as shown in Fig. 5c. The large particles at the grain boundaries do not show as much evidence of associated dislocation activity. Mobile dislocations do not penetrate the precipitate rods but are slowed down at the boundary probably due to a high resistance inside the particle. Dipolar dislocation walls such as those within persistent slip bands (PSBs) in copper were observed in the PFZs as shown in Fig. 5d. The dislocation density in the PFZ was generally lower than the inter-band region. Shearing of large precipitate particles in the interior of the grains by matrix dislocations was observed leading to the formation of anti-phase boundaries (Fig. 5e). Occasional cracking of large precipitates was also observed (Fig. 5f). No shearing or cracking of the grain-boundary precipitates in the PFZs was observed.

4. Discussion

The evolution of dislocation structure in the grain interior and PFZs leading to cyclic saturation can be

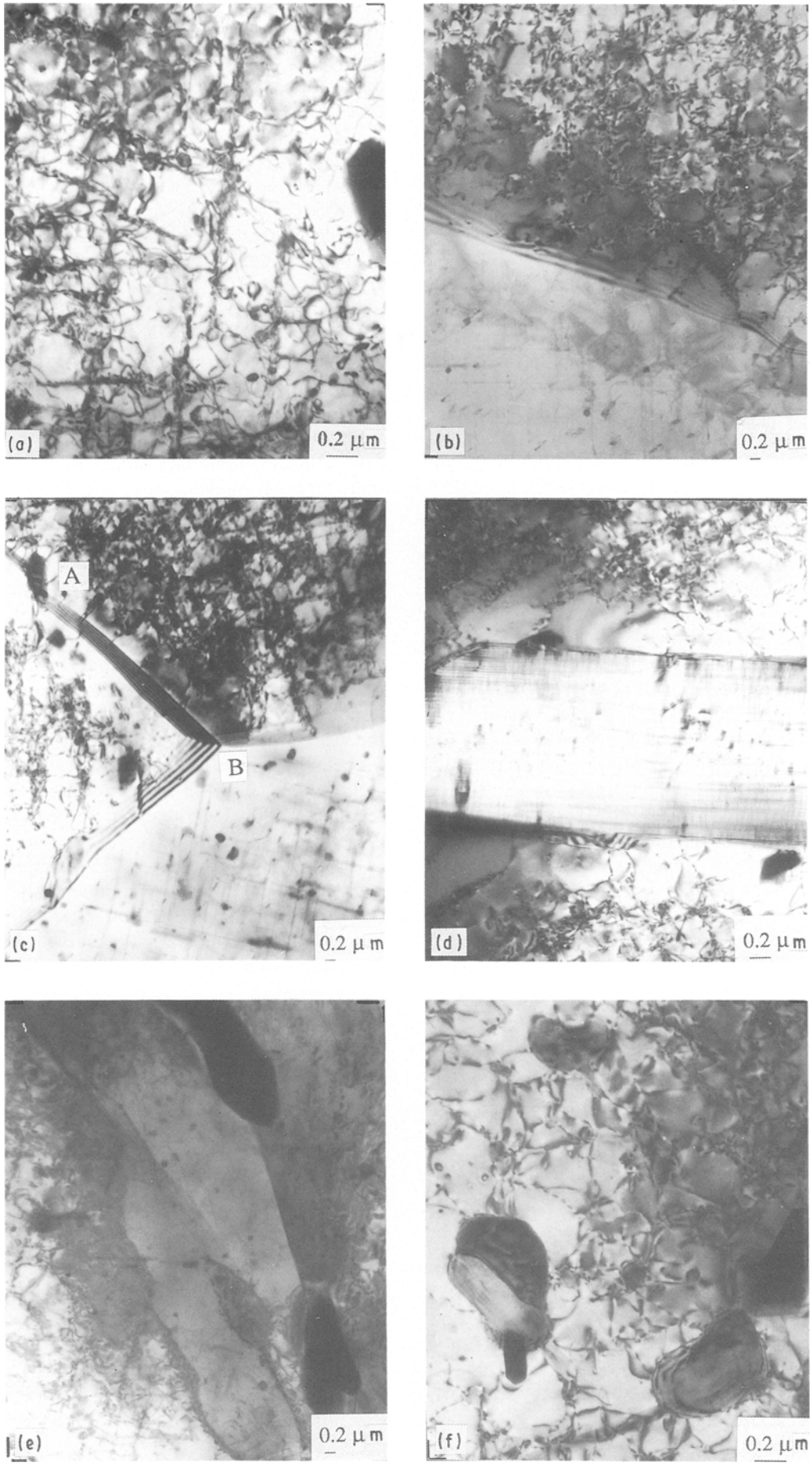

Figure 4 Transmission electron micrographs of cyclically deformed specimens in the cyclic hardening region at $\Delta\varepsilon/2 = 0.005$ and $\dot{\varepsilon} = 0.01\ s^{-1}$ after 30 cycles showing, (a) dislocation–precipitate grid structure in the grain interior, (b) dislocation structure in the PFZ, (c) dislocation structure at a grain triple point, (d) dislocation structure in the vicinity of a large Mg_2Si precipitate plate, (e) termination of dislocation bands at the PFZ boundary, (f) dislocation interaction with smaller precipitates.

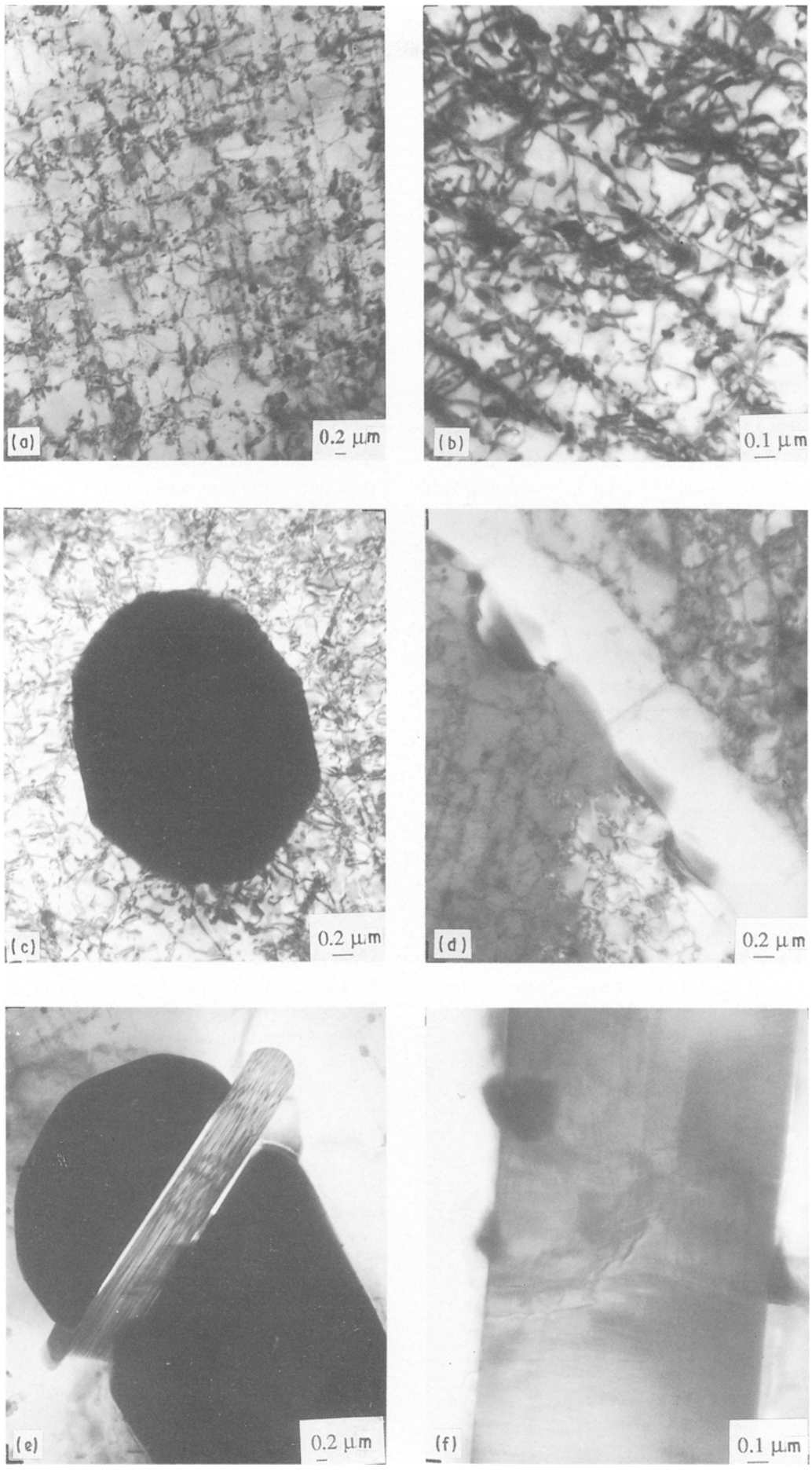

Figure 5 Transmission electron micrographs of a cyclically deformed specimen after 511 cycles at $\Delta\varepsilon/2 = 0.005$ and $\dot{\varepsilon} = 0.01\,s^{-1}$ showing, (a, b) well established dislocation–precipitate grid structure, (c) interaction of dislocations with a large spherical particle, (d) dislocation dipolar walls in a PFZ, (e) shearing of a large precipitate, (f) cracking of a large precipitate.

summarized as follows. The dislocation density is uniformly low prior to cycling throughout the specimen. Dislocation generation during the first cycles lead to an increase in the dislocation density in the grain interior. Screw dislocation motion, multiplication, and mutual interaction within the β′ rods leads to the formation of jogs on screw dislocations. Dislocation clusters, built up of edge multipoles, and debris appear between the β′ rods while the free dislocations approach the β′ rod–matrix interfaces. The dislocations produced in the early stages of cycling are locked progressively by the precipitates and lead to a more planar arrangement of dislocations within the grains. The mean free path of dislocations in the grain interior where a closely spaced and ordered distribution of β′ precipitate rods exists is smaller than the statistically random distribution of a few large dispersoids and precipitates in the PFZs and grain interiors [22, 23]. It is therefore expected that the contribution of β′ precipitates to the slip mode and total dislocation density is large during initial stages of cycling. In the PFZs, the capacity of three-dimensional motion via cross-slip easily allows for the dislocation arrangement into wavy configurations. Also, in the vicinity of large β plates, extensive cross-slip of screw dislocations due to the absence of β′ rods leads to wavy slip configurations typical of pure aluminium. These observations are in agreement with the fatigue of Al–3%Cu alloy containing non-shearable θ′ plates [24] where a general tangling of dislocations with the precipitate plates has been observed when the plates are closely spaced. However, when the plates are widely apart, dislocation cells form in the matirx.

At large cycles, the mean free path of the dislocations between the β′ precipitates is progressively reduced and is considerably smaller than the geometric slip distance which depends on the shape and spacing of β′ rods. Consequently, statistically stored dislocation density may dominate the total dislocation density of the alloy [22, 23]. The dense tangled dislocations relieve the high stresses localized around the particles in order to make the plastically sheared state of the matrix compatible with the elastically deformed state of the particle. The essential characteristics of the microstructure in the steady state are shown schematically in Fig. 6.

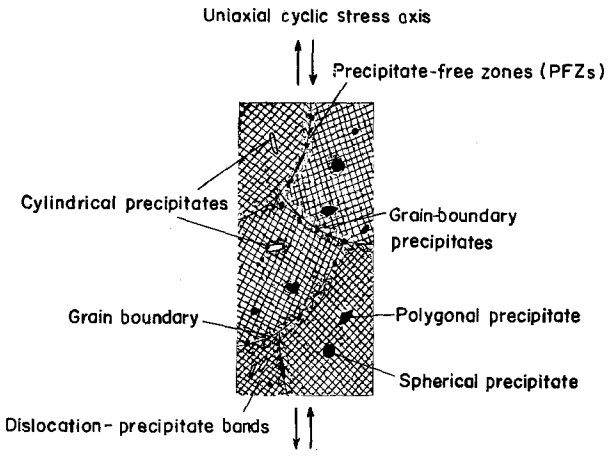

Figure 6 Schematic drawing of the microstructure formed after cyclic saturation.

Various observations during cyclic hardening and saturation stages can be broadly divided into kinematic (or directional) and isotropic mechanisms, i.e. mechanisms responsible for kinematic and isotropic hardening, respectively [21, 25]. Kinematic mechanisms observed include dispersion hardening due to the interaction of dislocations with precipitate particles, dislocation bowing between particles, dislocation looping and pile-ups at the large non-shearable precipitates and β′ rods, and dislocation multiplication within the matrix. Isotropic mechanisms observed include mechanisms involving the formation of jogs, tangles, and dislocation forests within the matrix between the β′-Mg_2Si precipitate rods and dislocation cells within the soft PFZs. Both kinematic- and isotropic-type mechanisms are responsible for the build up of inhomogeneous dislocation structure during cyclic hardening and saturation.

5. Conclusions

1. A continuous increase in the density of dislocations in the interior of the grains as well as in the PFZs is observed up to 30 cycles at a strain amplitude and strain rate of 0.005 and $1 \times 10^{-2} s^{-1}$, respectively, in the cyclic hardening region. The observations reveal no significant increase in the dislocation density in the region 30–511 cycles.

2. Dislocation tangling at β′-Mg_2Si precipitate rods contribute predominantly to cyclic hardening in the early stage. A stable dislocation band structure exists throughout the bulk of the specimen except at PFZs at high cycles. A more cell-like structure forms at the PFZs and in the vicinity of large β plates where the absence of precipitates tends to cause extensive cross-slip.

3. Various kinematic- and isotropic-type strengthening mechanisms operate during cyclic deformation of overaged Al–Mg–Si alloy such as Orowan dislocation looping, dislocation bowing, formation of jogs, tangles, and dislocation forests. The mechanisms are responsible for the build up of inhomogeneous dislocation structure during cyclic hardening and saturation.

Acknowledgements

The author thanks the Department of Mechanical Engineering, Washington University, St Louis for the award of a fellowship during his stay at the University. The comments and help with TEM work from Dr Phil Fraundorf, University of Missouri, St Louis, and Dr S. M. L. Sastry, McDonnell Douglas Research Labs, St Louis, and Dr K. K. Sankaran, McDonnell Aircraft Company, were appreciated.

References

1. C. CALABRESE and C. LAIRD, *Mater. Sci. Engng* **13** (1974) 141.

2. R. E. STOLTZ and R. M. PELLOUX, *Met. Trans.* **7A** (1976) 1295.
3. M. R. JAMES and A. W. SLEEWYK, *Acta Metall.* **26** (1978) 1721.
4. E. G. PLUMBRIDGE, E. G. ELLISON and K. T. NORMAN, *Metal Sci.* **17** (1983) 369.
5. J. LEE and C. LAIRD, *Phil. Mag. A* **47** (1983) 579.
6. J. H. DRIVER and P. RIEUX, *Mater. Sci. Engng* **68** (1984) 353.
7. H. D. CHANDLER and J. V. BEE, *Acta Metall.* **35** (1987) 2503.
8. W. J. BAXTER and T. R. McKINNEY, *Met. Trans.* **9A** (1988) 83.
9. L. HAUTEFEVILLE and M. CLAVEL, *Scripta. Metall.* **22** (1988) 1383.
10. C. CALABRESE and C. LAIRD, *Mater. Sci. Engng* **13** (1974) 159.
11. R. F. BRODERICK and G. A. SPIERING, *J. Metals* **7** (1972) 515.
12. R. J. ASARO, *Acta Metall.* **23** (1975) 1255.
13. M. H. JACOBS, *Phil. Mag.* **26** (1972) 1.
14. G. THOMAS, *J. Inst. Metals* **90** (1961–62) 57.
15. D. W. PASHLEY, J. W. RHODES and A. SANDOREK, *ibid.* **94** (1966) 41.
16. T. V. SHCHEGOLEVA, *Fiz. Metal. Metalloved* **25** (1968) 246.
17. A. L. TITCHNER and C. D. PONNIAH, in "Proceedings of the 3rd International Conference on the Strength of Metals and Alloys", Cambridge, UK, August 1973 (Institute of Metals and ISI, London) p. 432.
18. A. K. BUSBY, L. EDWARDS and J. W. MARTIN, in "Proceedings of the 2nd International Conference on Fatigue and Fatigue Thresholds", Birmingham, September 1984, edited by C. J. Beevers (Engineering Materials Advisory Services, Warley, 1984) p. 83.
19. K. PEDERSEN, in "Proceedings of the Conference, Fatigue '87", Charlottesville, VA, 28 June–3 July, 1987, edited by R. O. Ritchie and E. A. Starke Jr (Engineering Materials Advisory Services, Warley, 1987) p. 103.
20. B. MEIER and V. GEROLD, *ibid.*, p. 323.
21. M. JAIN, Fatigue and Fracture of Engineering Materials and Structures, in press.
22. M. F. ASHBY, *Phil. Mag.* **21** (1970) 399.
23. K. C. RUSSELL and M. F. ASHBY, *Acta Metall.* **18** (1970) 891.
24. B. K. PARK, V. GREENHUT, G. LUETJERING and S. WEISSMANN, Technical Report AFML-TR-70-195, August 1970.
25. G. J. WENG, *Acta Mech.* **37** (1980) 217.

Received 16 July 1990
and accepted 24 January 1991